Supplementary Material for Protocol dependent frictional granular jamming simulations: cyclical, compression and expansion

A. P. Santos[1,*], Ishan Srivastava[2], Leonardo E. Silbert[3], Jeremy B. Lechman[4], and Gary S. Grest[4]

[1]*AMA Inc., Thermal Protection Materials Branch, NASA Ames Research Center, Moffett Field, CA 94035, USA.*

[2]*Center for Computational Sciences and Engineering, Lawrence Berkeley National Laboratory, Berkeley, California 94720, USA.*

[3]*School of Math, Science and Engineering, Central New Mexico Community College, Albuquerque, NM 87106, USA.*

[4]*Sandia National Laboratories, Albuquerque, NM 87185, USA.*

[*]*Correspondance: andrew.p.santos@nasa.gov*

February 3, 2024

1 Initial kinetic energy impact on approach to packing

Figure 1 shows the role of the initial pressure on the approach to jamming in stress and microstructural properties. The figure in the main article, Figure 2, has box drag $f_{\rm drag} = 0.2$, while Figure 1 has no box drag $f_{\rm drag} = 0$ and different pressure. The time to pack increases and fluctuations decrease with increasing $f_{\rm drag}$ and decreasing pressure. These large fluctuations make the system less numerically stable as P_a decreases, which is why flow simulations, $\sigma_x y \neq 0$ for example, may need $f_{\rm drag} \neq 0$.

2 Non-monotonic volume fraction dependence for other methods

Figures 2 and 3 show the role of the initial pressure on packing methods I and II. At $t = 0$ packing method I starts at $\phi_0 = 0.05$, and a constant pressure $P_{a,f}$ is applied until the system jams. Packing method II first packs at an initial, high pressure $P_{a,0} > P_{a,f}$, and then the target pressure is instantaneously decreased to $P_{a,f}$. Figures 2 and 3 also show packings with more overcompression pressures $P_{a,i}$ for comparison. These figures demonstrate the distance from jamming for both the volume fraction and pressure affect the final microstructure.

3 Role of friction

Figure 4 shows the role of friction on the $\phi(P_a)$ depth, where as the coordination number is monotonic regardless of friction and the initial pressure. Figure 4 also demonstrates that the exact stress-tensor definition does not statistically change ϕ or Z.

Figure 5 demonstrates that at high pressures, pressure has a more dramatic role than friction on the packing volume fraction. However at those volume fractions real particles could break, and have large overlaps. Overlaps at $P = 10^{-6}$ are small $\delta < 0.000001d$, but at $P = 10^{-1}$ overlaps can be up to $\delta < 0.2d$, for example. The packing

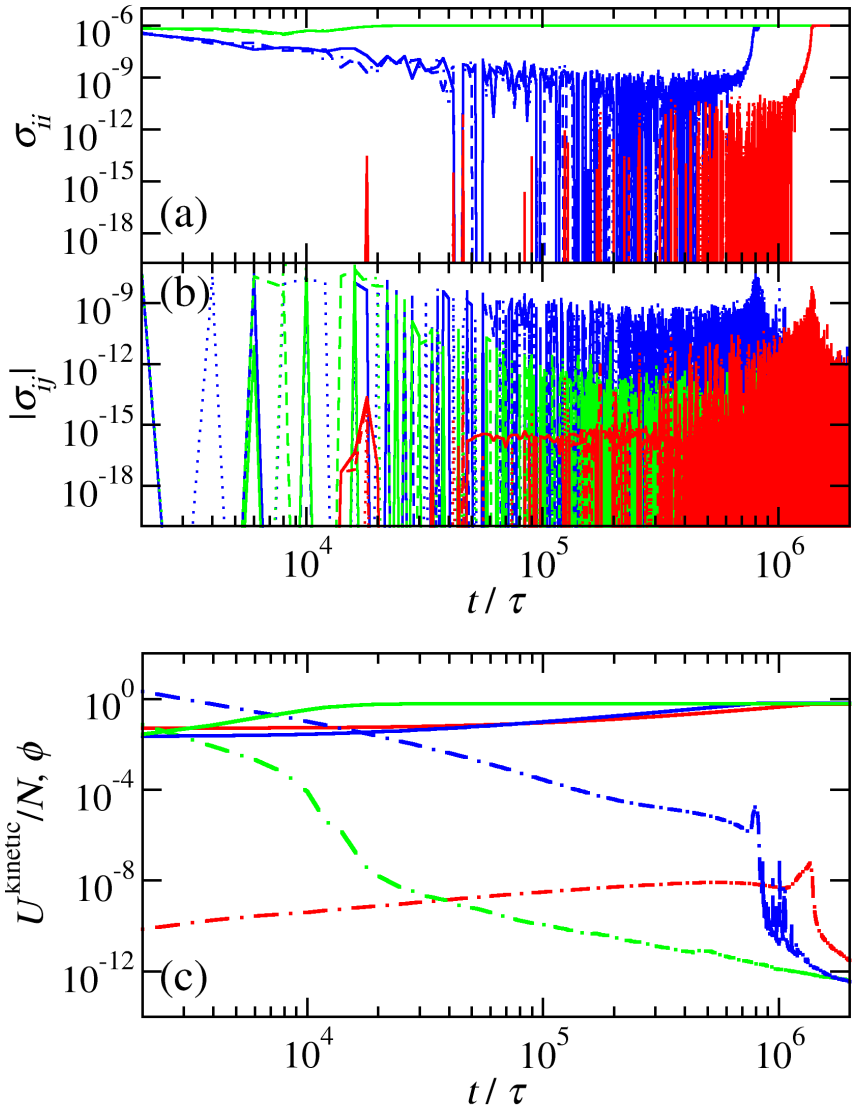

Figure 1: The (a) diagonal and (b) off-diagonal components of the applied stress tensor for $P_a = 10^{-6}$ for three different initial pressures $P_0 = 0$ (red) $P_0 = 10^{-4}$ (blue) and $P_0 = 10^{-2}$ (green). The different components of the stress tensor are plotted as different line types: xx, xy (solid lines), yy, xz (dashed lines) and zz, yz (dotted lines). The off-diagonal components of the stress tensor are shown as averages over 10 timesteps for clarity. (c) The kinetic energy (dot-dashed lines) and the volume fraction (solid) as a function of time For (a), (b) and (c) the box parameters are $P_{\mathrm{damp}} = 2.25$ and $f_{\mathrm{drag}} = 0$, and the friction state is $\mu_s = 0.2$.

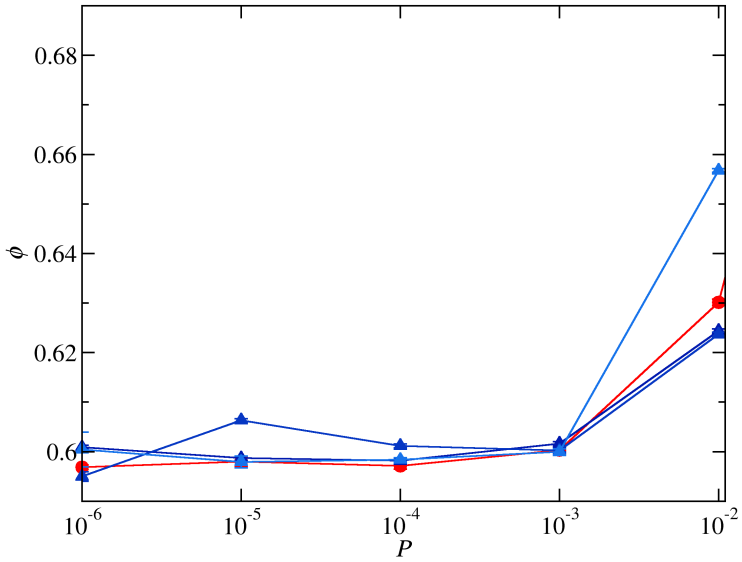

Figure 2: Packing fraction as a function of the pressure $\phi(P_a)$ for method I (red circles) and II (blue triangles) with no initial pressure $P_0 = 0$. Method II, where $P_{a,0}$ is varied from 10^{-4} (dark blue triangles), 10^{-3} (medium blue triangles) and 10^{-1} (light blue triangles). The box parameters are $P_{\rm damp} = 2.25$ and $f_{\rm drag} = 0$. Uncertainties are calculated from 6 different packings of $N = 10^4$ particles are similar in size to the symbols.

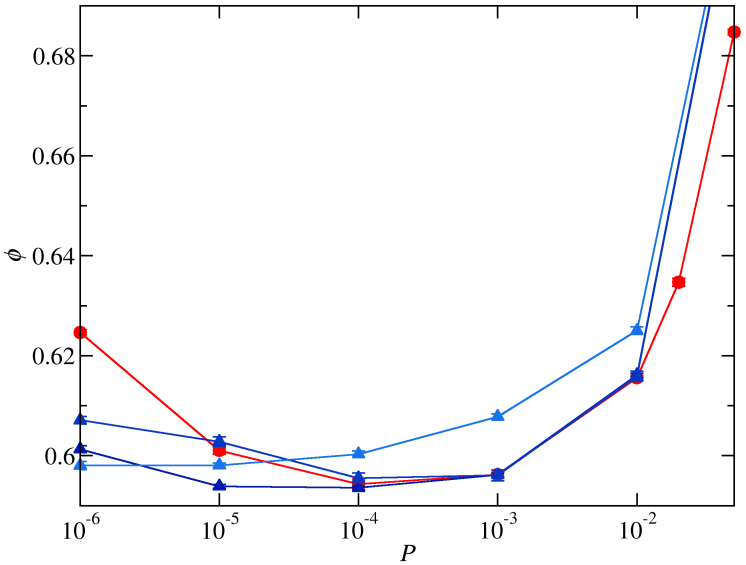

Figure 3: Packing fraction as a function of the pressure $\phi(P_a)$ for method I (red circles) and II (blue triangles) with no initial pressure $P_0 = 10^{-2}$. Method II, where $P_{a,i}$ is varied from 10^{-4} (dark blue triangles), 10^{-3} (medium blue triangles) and 10^{-1} (light blue triangles). The box parameters are $P_{\rm damp} = 2.25$ and $f_{\rm drag} = 0$. Uncertainties are calculated from 6 different packings of $N = 10^4$ particles are similar in size to the symbols.

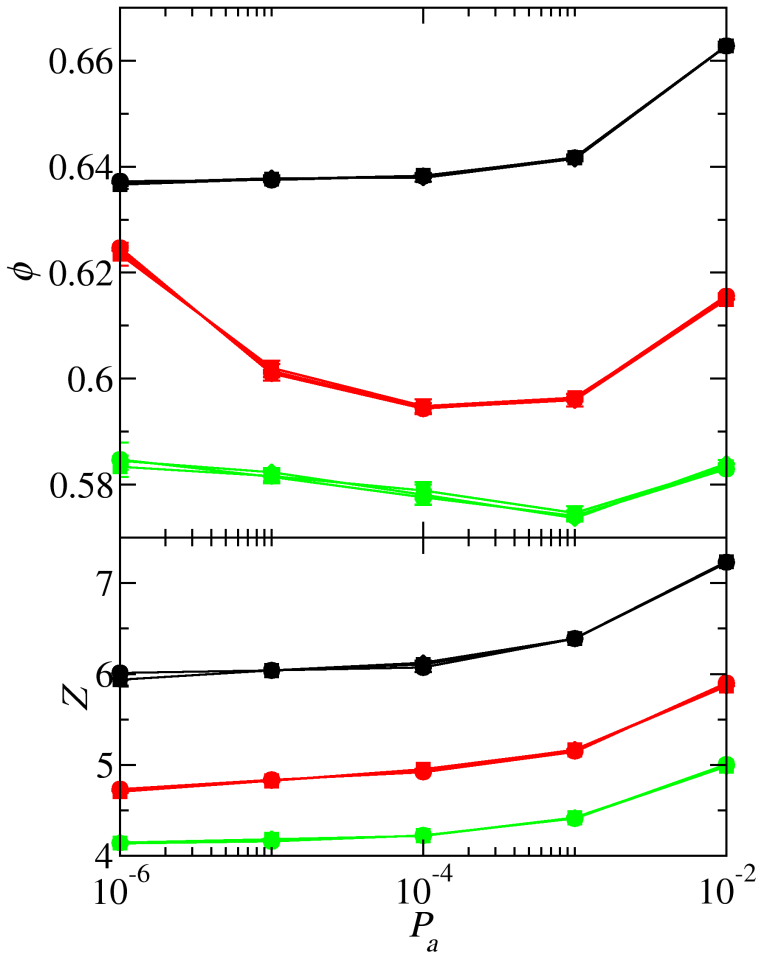

Figure 4: Packing fraction ϕ (top) and average coordination number without rattlers Z (bottom) as a function of the pressure for sliding frictions $\mu_s = 0.0$ (black), 0.2 (red) and 1 (green) with non-zero initial pressure $P_0 = 1.5 \times 10^{-2}$. Different constraints on the applied stress satisfied at jamming are shown: (i) $\sigma_{a,xx} = \sigma_{a,yy} = \sigma_{a,zz} = P$ and $\sigma_{a,xy} = \sigma_{a,yz} = \sigma_{a,xz} = 0$ (circles), (ii) $(\sigma_{a,xx} + \sigma_{a,yy} + \sigma_{a,zz})/3 = P$ and $\sigma_{a,xy} = \sigma_{a,yz} = \sigma_{a,xz} = 0$ (squares), and (iii) $\sigma_{a,xx} = \sigma_{a,yy} = \sigma_{a,zz} = P$ in an perfect orthorombic cube, where $\sigma_{a,xy}, \sigma_{a,yz}$ and $\sigma_{a,xz}$ are not set (diamonds). The symbols for the three jamming states overlap. These packings were generated with method I, $P_{\rm damp} = 2$ and $f_{\rm drag} = 1$. Uncertainties are calculated from 6 different packings of $N = 10^4$ particles are similar in size to the symbols.

volume fraction calculation $\phi = \frac{N_{\text{particle}} V_{\text{particle}}}{V_{\text{cell}}}$ does not subtract the overlap volumes, and overestimates the packing volume fraction, particularly for higher pressures $P \geq 10^{-1}$.

In the main text, the distribution of forces showed different behavior of sliding-to-normal contact force ratio near unity. The distribution of forces when comparing method I and II with initial kinetic pressure shows similar behavior as the main text example. The distributions of sliding forces, normalized by their maximum $\mu_s F_n$, are shown in Figure 6 for methods I and II. Both have non-zero initial pressure; method I has the non-monotonic $\phi(P_a)$ and method II does not. The impact of the $\phi(P_a)$ non-monotonicity is visible in $P(F_s/\mu_s F_n)$ for $P_a \leq 10^{-4}$. For method I, contacts near the Coulomb criteria ($F_s/\mu_s F_n > 0.94$) become less likely as pressure decreases from $P_a = 10^{-4}$ to $P_a = 10^{-6}$, Figure 6a. For method II, which does not show non-monotonicity in $\phi(P_a)$, contacts are more likely to be near the Coulomb criteria as the pressure decreases, Figure 6b. Method II shows the more expected behavior because $P_a \propto F_n$.

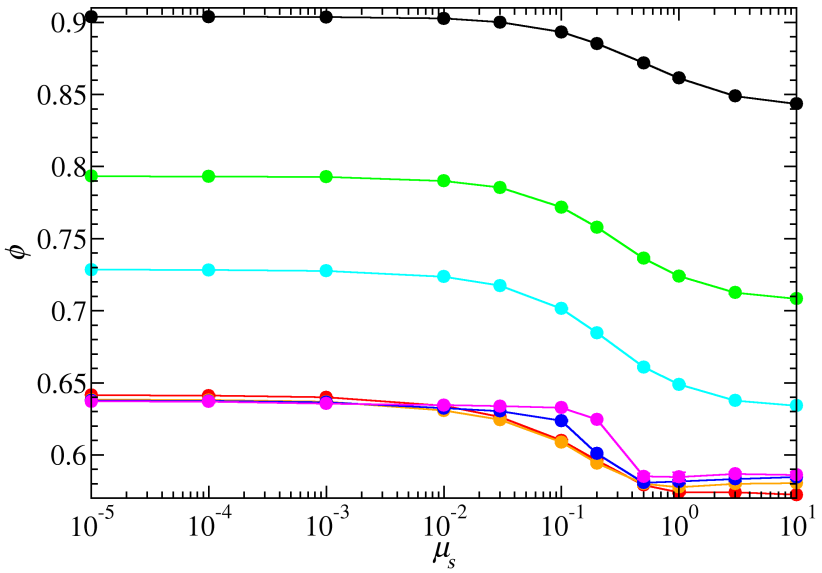

Figure 5: Packing fraction ϕ as a function of sliding friction coefficient μ_s with non-zero initial kinetic energy contribution to pressure $\langle P_i^{\text{kinetic}} \rangle = 9.6 \times 10^{-4}$. Different pressures are shown, $P_a = 2\text{x}10^{-1}$ (black), $1\text{x}10^{-1}$ (green), $5\text{x}10^{-2}$ (cyan), 10^{-3} (red), 10^{-4} (orange), 10^{-5} (blue) and 10^{-6} (magenta). Packings were generated using Method I and protocol parameters $P_{\text{damp}} = 2$, $f_{\text{drag}} = 0.1$.

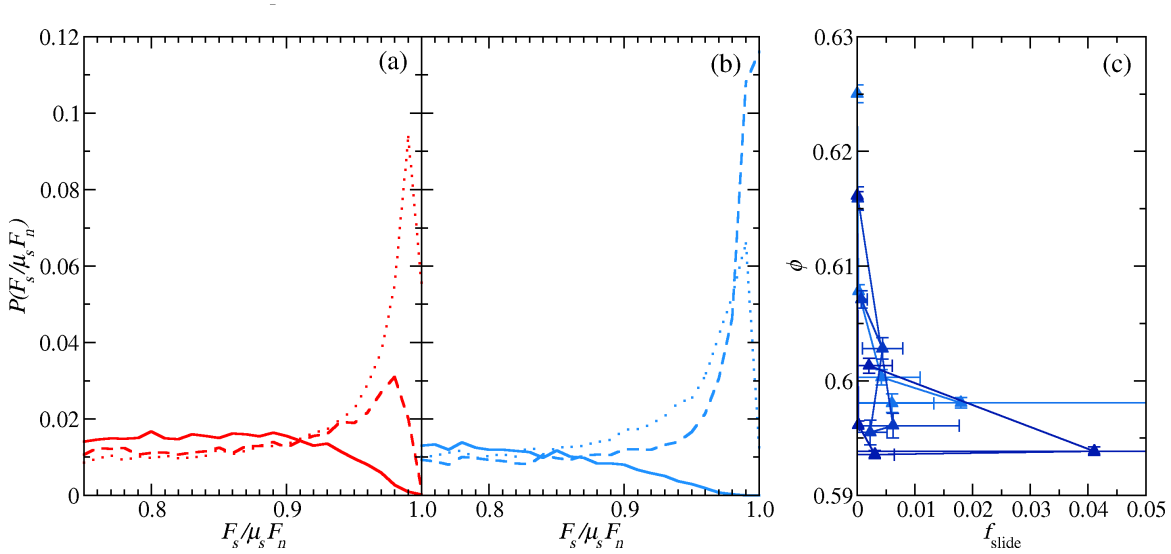

Figure 6: Probability distribution of the sliding force normalized by the maximum, $\mu_s F_n$, for different pressures: $P_a = 10^{-2}$ (solid lines), 10^{-4} (dotted lines) and 10^{-6} (dashed lines). (c) The volume fraction as a function of the fraction of contacts at the sliding friction criteria $\mu_s F_s = F_n$. The packings were generated with an initial pressure and protocol parameters $P_{\rm damp} = 2$, $f_{\rm drag} = 0.1$. The different colors of blue correspond to different values of $P_{a,0}$= 10^0 (light blue) and 10^{-3} (dark blue). Large uncertainties in $f_{\rm slide}$ are due to small absolute denominator values. This data corresponds to the case with an non-zero initial kinetic energy contribution to pressure $\langle P_i^{\rm kinetic} \rangle = 9.6 \times 10^{-4}$.